

# X-ray observations of the galaxy cluster PKS 0745–191: to the virial radius, and beyond

M. R. George,<sup>1</sup>★† A. C. Fabian,<sup>1</sup> J. S. Sanders,<sup>1</sup> A. J. Young<sup>2</sup> and H. R. Russell<sup>1</sup>

<sup>1</sup>*Institute of Astronomy, Madingley Road, Cambridge CB3 0HA*

<sup>2</sup>*H. H. Wills Physics Laboratory, University of Bristol, Tyndall Avenue, Bristol BS8 1TL*

Accepted 2009 January 22. Received 2009 January 22; in original form 2008 July 8

## ABSTRACT

We measure X-ray emission from the outskirts of the cluster of galaxies PKS 0745–191 with *Suzaku*, determining radial profiles of density, temperature, entropy, gas fraction and mass. These measurements extend beyond the virial radius for the first time, providing new information about cluster assembly and the diffuse intracluster medium out to  $\sim 1.5 r_{200}$  ( $r_{200} \simeq 1.7 \text{ Mpc} \simeq 15 \text{ arcmin}$ ). The temperature is found to decrease by roughly 70 per cent from 0.3 to  $1 r_{200}$ . We also see a flattening of the entropy profile near the virial radius and consider the implications this has for the assumption of hydrostatic equilibrium when deriving mass estimates. We place these observations in the context of simulations and analytical models to develop a better understanding of non-gravitational physics in the outskirts of the cluster.

**Key words:** galaxies: clusters: general – galaxies: clusters: individual: PKS 0745–191 – X-rays: galaxies: clusters.

## 1 INTRODUCTION

The outskirts of galaxy clusters present an opportunity to study the formation of large-scale structure as it happens. Beyond the core where non-gravitational processes such as cooling flows and feedback from active galactic nuclei (AGN) can dominate activity, clusters are expected to be more relaxed and to follow self-similar scaling relations (Kaiser 1986). The virial radius can be thought of as a border between regions of equilibration and infall, so merger activity from accreting material may play an important role in the outer dynamics.

As the largest virialized systems in the Universe, clusters of galaxies can be useful in constraining cosmological models. The position of clusters at the high end of the mass spectrum and their evolution from the initial density perturbations makes them sensitive probes of the scale of these fluctuations,  $\sigma_8$ , and the density of matter in the Universe,  $\Omega_m$  (White et al. 1993; Eke, Cole & Frenk 1996). Additionally, the evolution with redshift of cluster properties such as the gas mass fraction can be used to study other portions of the cosmic energy density budget (e.g. Allen et al. 2008). For a review of the cosmological importance of galaxy clusters, see Voit (2005).

To understand cluster properties, it is important that the relationships between observables and derived quantities are well calibrated. A common example is that temperature and density profiles

can be measured from X-ray spectra and used to determine a cluster’s mass under the assumptions of spherical symmetry and hydrostatic equilibrium between the gas pressure and gravitational potential. Though numerical simulations predict a decline in temperature towards the virial radius (e.g. Evrard, Metzler & Navarro 1996; Frenk et al. 1999; Loken et al. 2002), observations at smaller radii have produced inconsistent results. Some analyses have found declining profiles (e.g. Markevitch et al. 1998; De Grandi & Molendi 2002; Vikhlinin et al. 2005; Pratt et al. 2007), while others have seen a scattering of slopes consistent with flat or even increasing profiles (e.g. Irwin, Bregman & Evrard 1999; Zhang et al. 2004; Arnaud, Pointecouteau & Pratt 2005). These studies typically do not measure the temperature profiles much further out than half the virial radius, even with *Chandra* and *XMM*. Different methods of estimating the virial radius, using either scaling relations or direct determination from the mass profile, make comparisons difficult, but very few measurements have been made of cluster gas temperatures out to the virial radius (e.g. Solov'yeva et al. 2007; Reiprich et al. 2008), and to our knowledge none has been reported beyond it.

Until recently, X-ray detectors have been unable to measure the temperature of the intracluster medium (ICM) out to the virial radius due to its low surface brightness in the outskirts relative to background noise. Typically a mass profile such as that of Navarro, Frenk & White (1997, hereafter NFW) is used to extrapolate mass estimates to distances greater than those observed. One aim of our work is to measure properties of the ICM out to the virial radius in order to check the reliability of such extrapolations. For our purposes, we equate the virial radius with  $r_{200}$ , the radius within

★E-mail: mgeorge@astro.berkeley.edu

†Present address: Department of Astronomy, University of California, Berkeley, CA 94720, USA.

which the mean total density is 200 times the critical density of the Universe at the redshift of the cluster.

The low orbit of *Suzaku* places it within the Earth's magnetopause, giving it a significantly lower and more stable particle background compared to *Chandra* and *XMM-Newton*. Reiprich et al. (2008) have recently leveraged this ability for low surface brightness observations in the outskirts of A2204, measuring the temperature nearly to  $r_{200}$ . Other cluster observations with *Suzaku* have demonstrated its capacity for temperature and abundance measurements (e.g. Sato et al. 2007), providing an outline for some of the methods used here.

In this work, we present *Suzaku* observations of PKS 0745–191, a relaxed, cool core cluster that is the brightest in X-rays beyond  $z = 0.1$  (Fabian et al. 1985; Edge et al. 1990; Allen, Fabian & Kneib 1996). Previous measurements have found a mean gas temperature in the range of 6.4–8.5 keV, depending on the models used and regions studied (Chen, Ikebe & Böhringer 2003, and references therein). Allen et al. (1996) find good agreement between the central mass from X-rays and that determined from a strongly lensed arc, but the results of Chen et al. (2003) disagree, finding a factor of 2 smaller mass from *XMM* data (see also Snowden et al. 2008, for a re-analysis of the *XMM* data). We describe our observations in the next section, followed by details of the spectral analysis in Section 3, and the resulting profiles in Section 4. In Section 5 we place our findings in the context of other cluster studies, and we conclude the paper in Section 6. For distance scales, we use the cosmological parameters  $H_0 = 70 \text{ km s}^{-1} \text{ Mpc}^{-1}$  and  $\Omega_m = 1 - \Omega_\Lambda = 0.3$ , giving an angular scale of  $113 \text{ kpc arcmin}^{-1}$  at the cluster's redshift,  $z = 0.1028$ . The plotted and quoted error ranges are  $1\sigma$  statistical uncertainties except where otherwise stated.

## 2 OBSERVATIONS AND DATA REDUCTION

*Suzaku* observations of PKS 0745–191 were taken between 2007 May 11 and 14 in five separate fields of roughly 32 ks each. Details of these pointings are listed in Table 1. The central pointing is aimed toward the peak of the cluster emission and the others are positioned adjacently, with 4-arcmin overlap at each chip edge, as in Fig. 1. We use only data from the X-Ray Imaging Spectrometer (XIS; Koyama et al. 2007). We exclude the back-illuminated detector, XIS1, despite its higher sensitivity at low energies, because it also has a significantly higher particle background level than the two front-illuminated sensors, XIS0 and XIS3, which have similar responses. There is an offset between the measured temperatures of the BI and FI chips, and we discuss this contribution to our systematic uncertainties in Section 4.3. We simultaneously analyse data from the two FI sensors to effectively double the exposure time while keeping the noise low. Observations were taken in normal clocking and editing modes with spaced-row charge injection on, and the data have been processed with the energy scale calibration of v2.1.6.16. The data preparation described below was carried out using XSELECT 2.4.1 and FTOOLS version 6.5.1 from HEASARC

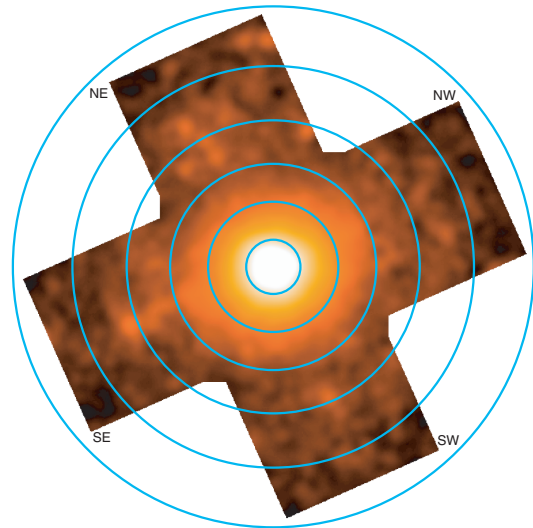


**Figure 1.** Exposure-corrected mosaic of PKS 0745–191, smoothed with a Gaussian of radius 1 arcmin. Background subtraction and vignetting correction have been omitted, and calibration regions and point sources have not yet been excised. Ring radii are 2.5, 6, 9.5, 13.5, 18.5 and 24 arcmin.

(High Energy Astrophysics Science Archive Research Center), with instrumental parameters from CALDB updated 2008 September 5. Updates to the calibration parameters released during the preparation of this paper do not affect the results beyond the statistical uncertainties.

We performed the standard screening of events files to remove time intervals during satellite manoeuvres, telemetry saturation and passage through the South Atlantic Anomaly, as well as elevation angles less than  $5^\circ$  and  $20^\circ$  from the nighttime and daytime Earth. The light curve for the remaining time intervals is stable, showing no sign of flaring or excess particle background. We exclude the corners of the detectors where  $^{55}\text{Fe}$  calibration sources lie, and obvious point sources seen in *Suzaku* or *XMM* images were excised with circular regions of radius 2.5 arcmin to remove more than 99 per cent of the flux spread by the point spread function (PSF). Detector response matrices and effective area functions are constructed with XISRMFGEN and XISSIMARFGEN (Ishisaki et al. 2007), respectively. The latter tool generates the spectral response for a given sky brightness, accounting for the known issue of contamination on the optical blocking filter. Uncertainties in this contamination should not affect our results significantly, as we do not consider energies below 1 keV. Vignetting effects will be different for cluster and background emission components, so we use a uniform surface brightness out to a radius of 20 arcmin when modelling the background emission and input a  $\beta$ -model surface brightness profile using the parameters of Chen et al. (2003) for the auxiliary response file applied to the cluster emission model. We find that modifying the parameters of the surface brightness profile used to determine the ‘effective area’ with XISSIMARFGEN does not significantly impact the output. Thus, we do not expect an unresolved central cusp or uncertainties from the outward extrapolation of the surface brightness profile to influence our results.

### 2.1 Background subtraction and modelling

Accounting for background emission is critical when observing regions of low surface brightness, and it consists of multiple

**Table 1.** Observational parameters of the five pointings.

Obs. ID	Position	Exposure (ks)	RA	Dec. (J2000)
802062010	Centre	32.0	116.8852	−19.2901
802062020	NW	32.2	116.6543	−19.2063
802062030	NE	30.8	116.9737	−19.0727
802062040	SE	32.9	117.1155	−19.3739
802062050	SW	33.4	116.7966	−19.5079

components. We subtract the non-X-ray background (NXB) of charged particles and gamma rays with XISNGBGEN (Tawa et al. 2008), which models the trend of these events from night Earth data, weighted by the magnetic cut-off rigidity. The X-ray background consists of solar wind charge exchange, thermal emission mainly from the hot local bubble and the Galactic halo and the cosmic X-ray background (CXB) due to unresolved point sources. Charge exchange contaminates the low-energy spectrum with emission lines that can vary on a time-scale of 10 min (Fujimoto et al. 2007), while the diffuse thermal emission and CXB are expected to be more stable and easily modelled. At the low Galactic latitude of this source ( $b = 3^\circ$ ), the soft thermal background could vary significantly with position. We opt to exclude the high-energy end of the spectrum where the NXB component dominates with several emission lines, and to also ignore the low-energy end where charge exchange and local thermal emission muddle the data, leaving the 1–5 keV band for consideration. Since the central regions have temperatures higher than the upper limit of the energy band used, we test that they are consistent with temperatures measured in a 1–8 keV band. Systematic uncertainties due to particle background subtraction at high energies and Galactic and other low-energy background components are discussed in Section 4.3. We opt for the narrower energy range to optimize the signal-to-noise ratio for whole cluster.

Since cluster emission fills the observed field, we cannot use detector regions from these pointings to subtract the remaining background. Instead, we analyse *Suzaku* data from the Lockman Hole (observation ID 102018010) taken only 8 days prior to the start of our observations. Despite the large difference in absorbing column density measured from H I maps ( $N_{\text{H}} = 5.7 \times 10^{19} \text{ cm}^{-2}$  for the Lockman Hole versus  $4.2 \times 10^{21} \text{ cm}^{-2}$  for PKS 0745–191; Kalberla et al. 2005), *ROSAT* observations (Snowden et al. 1997) detect similar background levels from 1 to 2 keV at the two positions. We find that the Lockman Hole data from 0.5 to 8 keV is well modelled by a power law of photon index 1.4, absorbed by the column density measured by the H I maps, added to an unabsorbed MEKAL thermal plasma model (Mewe, Gronenschild & van den Oord 1985; Mewe, Lemen & van den Oord 1986; Liedahl, Osterheld & Goldstein 1995) at 0.1 keV with solar metallicity using the relative abundances of Anders & Grevesse (1989), allowing only the normalizations to vary. The best-fitting normalizations in the 1–5 keV range are  $7.26 \times 10^{-4} \text{ photon keV}^{-1} \text{ cm}^{-2} \text{ s}^{-1}$  at 1 keV for the CXB and  $0.78 \text{ cm}^{-5} \text{ arcmin}^{-2}$  for the soft thermal component.<sup>1</sup> We do not find an improvement in the fit with another low-temperature component, as is often used (e.g. Vikhlinin et al. 2005). We note that in the 1–5 keV band used here, the fit is not even particularly sensitive to the normalization of the remaining soft thermal component, but we include it as an empirical description of the background model to be applied to the PKS 0745–191 data. We attempted to fit the outermost regions of the cluster observations with a similar model and an added low-temperature ( $\sim 0.25 \text{ keV}$ ) Galactic component. The normalizations required are much higher than for the Lockman Hole and would be inconsistent with the *ROSAT* observations for this source. The fit to the outer regions of PKS 0745–191 is improved with a higher temperature component ( $\gtrsim 1.5 \text{ keV}$ ), indicative of cluster emission covering the entire field.

<sup>1</sup> We follow Sato et al. (2007) in dividing the surface brightness normalization of the thermal component by the solid angle used in the ancillary response file generation,  $\Omega = 20 \text{ arcmin}$ , so that  $\text{Norm} = 10^{-20} \int n_e n_H dV / [4\pi(1+z)^2 D_A^2] / \Omega$  in  $\text{cm}^{-5} \text{ arcmin}^{-2}$ , where  $D_A$  is the angular diameter distance to the cluster.

### 3 SPECTRAL ANALYSIS

Spectra were extracted in annular regions of radii 0–2.5, 2.5–6, 6–9.5, 9.5–13.5, 13.5–18.5 and  $> 18.5 \text{ arcmin}$ , with the outermost region reaching to nearly  $24 \text{ arcmin}$ . For each annulus we define an effective radius that is approximately an emission-weighted mean (McLaughlin 1999),  $r = [0.5(r_{\text{in}}^{3/2} + r_{\text{out}}^{3/2})]^{2/3}$ . These regions are centred at right ascension and declination 07:47:31.325,  $-19:17:39.95$  (J2000), which is coincident with the cD galaxy and both the peak and centroid of X-ray emission. Because of the low count rates in some channels, we use the Cash (1979) C statistic.

We used XSPEC v12.5.0 to simultaneously fit models of the spectra, with data from each pointing grouped by annulus unless specified otherwise. We first subtract the NXB spectra from identical regions on the detector, scaled by the relative exposure time of the night Earth observations. Next, we model the local thermal emission and CXB components, fixed to the best-fitting values from the Lockman Hole observations. Finally, we model the remaining emission, that from the cluster, with another MEKAL component at the cluster’s redshift,  $z = 0.1028$ . We fix the column density absorbing the cluster and CXB components to the best-fitting value at the centre,  $N_{\text{H}} = 3.6 \times 10^{21} \text{ cm}^{-2}$ , which is lower than the H I measurement but consistent with the value from *XMM*’s EPN (Chen et al. 2003). We allow the metallicity to vary in the centre but fix it to  $0.3 Z_\odot$  at larger radii. Of the remaining parameters, only the temperature and normalization of the thermal ICM component are allowed to vary.

The broad PSF of *Suzaku*, with a half-power diameter of  $\sim 2 \text{ arcmin}$ , will cause some emission from each annulus on the sky to be distributed into others on the detector. We correct for this effect following the method of Sato et al. (2007), who importantly show that *Suzaku*’s PSF is nearly energy independent. We use a circularly symmetric  $\beta$ -model with the best-fitting parameters of Chen et al. (2003), consistent with the surface brightness profile observed here, and a monochromatic energy of 1.5 keV to generate a photon list that is propagated with a ray-tracing simulator (XISSIM) through the detector optics. For each annulus on the sky, we use the ratio of flux landing in the corresponding detector annulus to the flux in each other annulus to calculate cross-annuli normalization factors. In the spectral model, we add a thermal component from each annulus to every other annulus with the temperature tied to the original region and the normalization scaled by these factors. The relative contributions to each annulus from other annuli, as derived from these PSF correction factors and the best-fitting normalizations, are given in Table 2. The model was fitted simultaneously over all annuli and resulted in an excellent fit; the C statistic, though not a direct measure of goodness of fit, was 65 413 using 98 640 bins and 98 627 degrees of freedom. The spectra and models are shown in Figs 2 and 3. We note that the individual spectra are fitted simultaneously, and are only combined by annular regions in these figures for visual clarity.

### 4 RESULTS

#### 4.1 Temperature, density and entropy profiles

Temperature and density profiles are the primary data products of X-ray observations of clusters, from which other properties including entropy, mass and gas fraction profiles can be derived. We obtain the density from the normalization of the best-fitting thermal plasma model which is proportional to the emission measure,  $\int n_e n_H dV$ , where  $n_e \approx 1.2 n_H$  for typical abundances. We use the simplifying

**Table 2.** Relative flux contributions due to PSF spreading. Values correspond to the fraction of flux measured in the detector region (columns) originating from the cluster region (rows), i.e. of the flux measured in the outermost annulus, we expect 88.1 per cent to come from the corresponding region in the sky, and only 0.1 per cent to have originated in the central projected region.

	0–2.5 arcmin	2.5–6 arcmin	6–9.5 arcmin	9.5–13.5 arcmin	13.5–18.5 arcmin	18.5–24 arcmin
0–2.5 arcmin	89.9	19.3	2.6	0.4	<0.05	0.1
2.5–6 arcmin	9.7	66.8	5.7	0.6	0.1	0.1
6–9.5 arcmin	0.3	13.1	84.4	7.8	0.6	0.1
9.5–13.5 arcmin	0.1	0.5	6.5	78.5	7.3	0.8
13.5–18.5 arcmin	<0.05	0.1	0.5	11.9	84.1	10.9
18.5–24 arcmin	<0.05	0.1	0.3	0.7	7.8	88.1

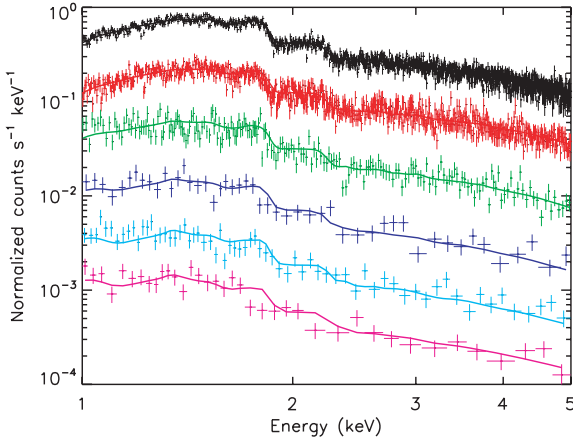


**Figure 2.** Data and spectral fits including PSF correction for each annular region, illustrating the softening of the spectra with increasing radius. The regions plotted are 0–2.5 arcmin (black), 2.5–6 arcmin (red), 6–9.5 arcmin (green), 9.5–13.5 arcmin (blue), 13.5–18.5 arcmin (cyan) and >18.5 arcmin (magenta). Data have been rebinned to a minimum significance of  $5\sigma$  for each point, and each spectrum has been arbitrarily renormalized for visual clarity.

assumption of constant density within each annulus, and estimate the volume as that of the intersection between cylindrical and spherical shells with shared inner and outer radii,  $V = (4\pi/3)(r_{\text{out}}^2 - r_{\text{in}}^2)^{3/2}$ , scaled by the fraction of the projected annulus observed. With the density and temperature determined, we can calculate the entropy profile,  $K = kT/n_e^{2/3}$ . Each of these profiles is shown in Fig. 4.

The cool core, though blurred by the wide PSF, is seen as a decrease in temperature near the centre. The more novel result is the clearly observed decline in temperature in the outskirts of the cluster. Excluding the core, this decline can be fit with a power law  $T(r) = T_0 r^{\alpha_T}$  with index  $\alpha_T = -0.94 \pm 0.06$ . The gas density profile can similarly be fit with a power law, excluding the central region again for uniformity, with index  $\alpha_n = -2.23 \pm 0.01$ . If we assume a polytropic distribution for an ideal gas,  $P \propto n_H kT \propto n_H^\Gamma$ , then we find  $\Gamma = 1 + (\alpha_T/\alpha_n) = 1.42 \pm 0.03$ . This value is higher than that found for cooling flow clusters determined by e.g. De Grandi & Molendi (2002), who measured  $\Gamma \simeq 1.2$  in the radial range  $0.2 < r \lesssim 0.6 r_{180}$ .

Gas with high entropy rises, so the radial entropy profile is expected to increase. Puzzlingly, the entropy profile we observe rises from the centre and then appears to level off beyond  $\sim 10$  arcmin, putting it on the border of convective instability. We will discuss possible explanations for this behaviour in later sections.

## 4.2 Mass profiles

To derive a mass profile, we assume that the gas properties are spherically symmetric and that the cluster is in hydrostatic equilibrium. Balancing the thermal pressure gradient against the gravitational potential, we obtain an expression for the total gravitating mass in terms of temperature and density:

$$M(<r) = \frac{-kr^2}{G\mu m_H n_H} \left( T \frac{dn_H}{dr} + n_H \frac{dT}{dr} \right). \quad (1)$$

We assume that the total density distribution can be described by an NFW profile:

$$\rho(r) = \frac{\rho_0}{r/r_s [1 + (r/r_s)]^2}, \quad (2)$$

where  $\rho_0$  is a density normalization and  $r_s$  is a scale radius related to the cluster's concentration,  $c_{200} \equiv r_{200}/r_s$ .

Following an approach similar to that of Schmidt & Allen (2007), we use an NFW model and the observed gas density distribution to predict a temperature in each annulus, beginning with the outermost bin. Density gradients are taken linearly between the radial bins, which reduce the correlation in uncertainties between non-adjacent data points that are created with other interpolations such as cubic splines, as some authors use (see Voigt & Fabian 2006, for a discussion). This approach could be improved with more radial bins, but the wide PSF of *Suzaku* and the low count rate in the cluster outskirts limit us from using thinner annular regions. To ensure that the outermost temperature value is robustly estimated, we take the median outer value of the profiles that best fit 100 Monte Carlo realizations of the observed temperature profile, normally distributed within its error bars. The model temperature profiles are similar if we begin at the innermost region, so the result is not particularly sensitive to the boundary values. Iterating over a range of NFW parameters, we select the mass model that produces the temperatures that best fit the observed profile.

In order to resolve the region within the NFW scale radius, we supplement the *Suzaku* data with an archival 20 ks *Chandra* observation (ID 2427) taken with the ACIS-S (Advanced CCD Imaging Spectrometer) detector in VFAINT (very faint) mode. These data were reduced following the description of O'Dea et al. (2008), with spectra extracted in circular annuli and deprojected using the method of Sanders & Fabian (2007). After using the outermost *Chandra* annulus to subtract contaminating flux from inner regions it is omitted from further analysis since it may contain external cluster emission, leaving six regions to replace the innermost *Suzaku* bin, where the temperature and density are in reasonable agreement with the *Chandra* data. We use *Chandra* data for its sharper PSF, but the *XMM* temperature profile in Snowden et al. (2008) is also consistent at the smaller radii of that observation.

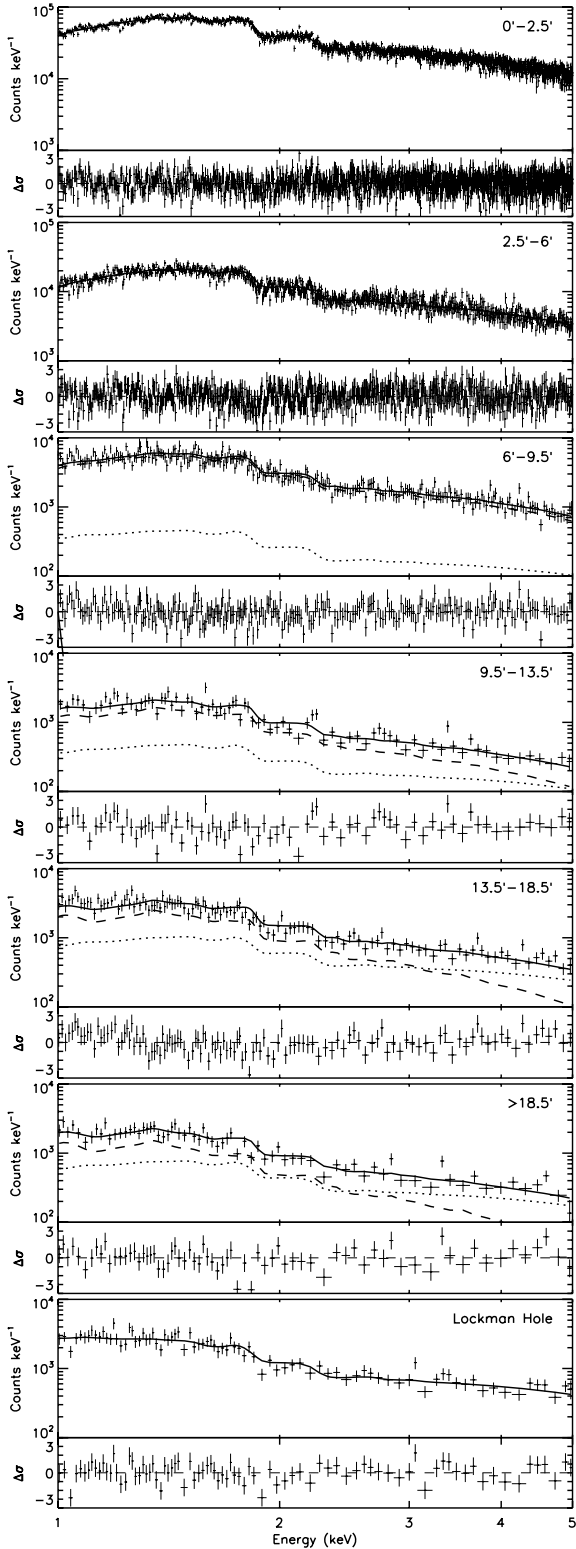


**Figure 3.** Same as Fig. 2, but with residuals to show the quality of the spectral fits, and with the Lockman Hole background spectrum included for comparison. Count levels have not been renormalized and we note that the regions have different areas and exposure times. Dotted and dashed curves represent the background (CXB+thermal) and cluster emission models, respectively.

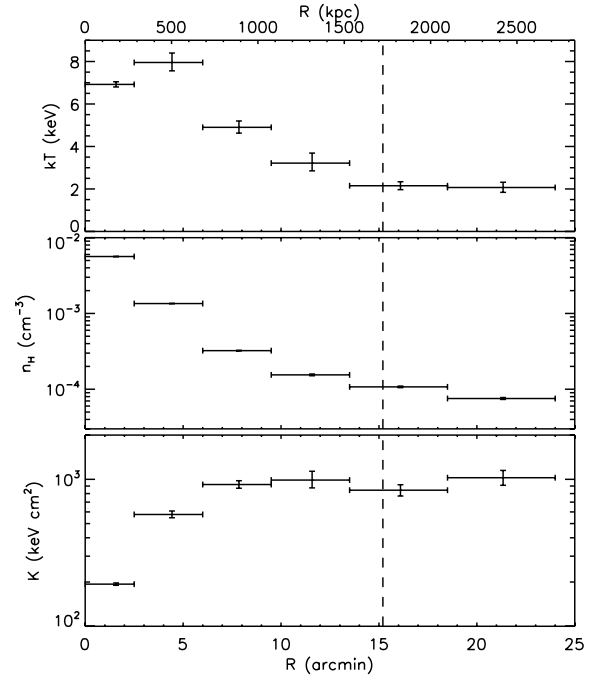


**Figure 4.** Projected temperature, density and entropy profiles. The vertical dashed line shows our estimate of  $r_{200}$ , derived in Section 4.2.

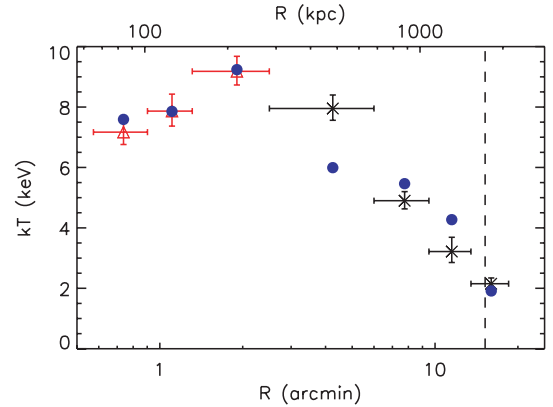


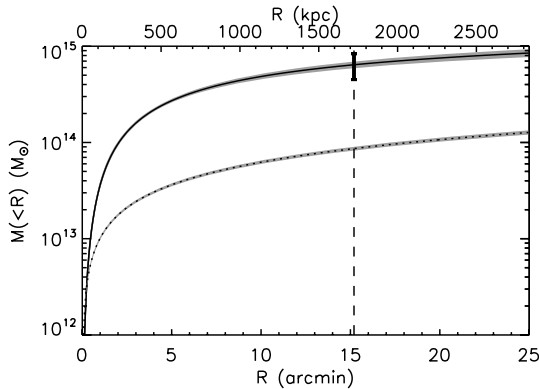
**Figure 5.** *Chandra* (red triangles) and *Suzaku* (black crosses) temperature values used in mass-fitting analysis, along with matching temperatures for best-fitting NFW profile (blue circles).

The model temperature profile, shown in Fig. 5, does not fit the data very well over all annuli, and the best fit to the observed temperatures ( $\chi^2 \approx 39$  for 7 degrees of freedom) is obtained after ignoring the outermost *Suzaku* bin which is beyond the virial radius where the assumption of hydrostatic equilibrium is expected to fail, and the *Chandra* regions in the cool core within  $\sim 70$  kpc of the centre where the gas is likely to be multiply phased. The main deviation in our data from this acceptable temperature fit arises from the 2.5–6 arcmin *Suzaku* annulus. Possible explanations include a PSF correction that could be too large, a cross-calibration issue between *Chandra* and *Suzaku*, or even non-gravitational heating in that region.

The resulting mass profile has best-fitting NFW parameters of  $c_{200} = 7.5^{+1.1}_{-0.9}$  and  $r_s = 230^{+40}_{-40}$  kpc, producing a virial radius  $r_{200} = c_{200}r_s = 1.72 \pm 0.06$  Mpc, or 15.2 arcmin and mass  $M_{200} = 200\rho_c(z)(4\pi/3)(r_{200})^3 = 6.4 \pm 0.6 \times 10^{14} M_\odot$ . We

**Table 3.** Concentration and virial mass determinations for PKS 0745–191, compiled by Comerford & Natarajan (2007) with values for this work added.

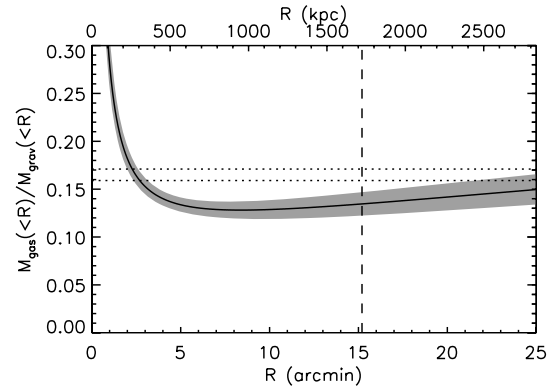
$c_{200}$	$M_{200}$ ( $10^{14} M_{\odot}$ )	Reference
$3.83^{+0.52}_{-0.27}$	$18.6^{+3.5}_{-4.0}$	Allen et al. (2003)
$5.12^{+0.40}_{-0.40}$	$10.0^{+1.2}_{-1.2}$	Pointecouteau, Arnaud & Pratt (2005)
$5.46^{+3.22}_{-2.88}$	$9.7^{+52.2}_{-8.5}$	Voigt & Fabian (2006)
$5.86^{+1.56}_{-1.07}$	$11.82^{+4.70}_{-3.55}$	Schmidt & Allen (2007)
$7.5^{+1.1}_{-0.9}$	$6.4^{+0.6}_{-0.6}$	This work

**Figure 6.** Cumulative profiles of gas mass (dotted lower curve) and total gravitational mass (solid upper curve) with  $1\sigma$  statistical error ranges in grey. The single error bar shows the 30 per cent systematic uncertainty on  $M_{200}$  and the vertical dashed line shows our estimate of  $r_{200}$ , derived in Section 4.2.

estimate total uncertainty on the virial mass, including systematics, of 30 per cent, which is described further in the next section. We compare these values with previous determinations in Table 3 and plot the mass profile in Fig. 6, along with the cumulative gas mass profile obtained from the power-law fit to the *Suzaku* gas density profile.

The NFW concentration is higher than previous estimates, and the virial mass we determine is lower, due in part to the smaller virial radius found in this work. Reiprich & Böhringer (2002) used an isothermal fit to *ROSAT* and *ASCA* data and found a value of  $1.95 \pm 0.03$  Mpc updated to the cosmological parameters we adopt. Schmidt & Allen (2007) found an even larger value for the virial radius, fitting an NFW profile to *Chandra* data in the central region to obtain  $r_{200} \approx 2.2$  Mpc. One issue with past NFW fits used to calculate the virial radius is that the data often do not extend even to the NFW scale radius, let alone the virial radius.

We can compare our mass profile with the projected mass determined from a strong lensing arc of radius 34.5 kpc seen with *Hubble* imagery by Allen et al. (1996). Updating their mass estimate for the circular lens model to account for the current cosmological parameters, we expect a mass of  $6.4 \times 10^{12} M_{\odot}$  projected within a cylinder along the line of sight of the centre of the cluster with a radius of the lensing arc, which is consistent with the statistical and systematic uncertainties of our best-fitting NFW model when integrating the mass in the cylinder out to  $r_{200}$ . We note that this includes an extrapolation of our profile into the core region where we have excluded data from our fit because of non-thermal processes. While it is reassuring to see this reasonable agreement between separate mass estimates, we caution that comparisons of this type

**Figure 7.** Gas fraction profile for PKS 0745–191, the ratio of the dotted to solid curves in Fig. 6, with  $1\sigma$  statistical error range in grey. Dotted lines show the  $1\sigma$  range around the value of  $\Omega_b/\Omega_m$  from Komatsu et al. (2008). The vertical dashed line shows our estimate of  $r_{200}$ , derived in Section 4.2.

of wide-field X-ray analysis with strong lensing data only involve a small fraction of the total cluster mass. Weak lensing analyses, which can provide mass projections over a much broader area, will provide important comparisons for virial mass estimates.

In Fig. 7, we plot the gas fraction profile, defined as the fraction of mass within a given radius composed of X-ray emitting gas. The gas fraction appears to rise slightly at the outer radii, consistent with the profile observed for PKS 0745–191 in *ROSAT* data by Allen et al. (1996). The values of the  $f_{\text{gas}}$  profile in the outskirts of this cluster are similar to recent measurements of the mean cosmic baryon fraction (Komatsu et al. 2009).

### 4.3 Uncertainties

A number of systematic uncertainties could add contributions to our error budget beyond the statistical ranges plotted. We summarize our estimates of several of these systematic uncertainties to the temperature profile, including the effects of PSF correction and renormalization of background components, in Table 4. The changes due to the PSF correction are mostly small, with the main effect being a  $\sim 12$  per cent increase in temperature in the second innermost annulus after accounting for emission from the cool gas in the core that has scattered outward. There is a significant uncertainty in the temperature of the central region because *Suzaku*'s PSF blurs the steep gradient of the cool core. As Reiprich et al. (2008) points out, the approach to PSF corrections described in the previous section does not fully account for this blurring within the central region, however, our method provides a reasonable approximation to the corrections needed.

To ensure that the background models used do not significantly impact the results, we vary the normalizations of these components and measure the deviations produced in temperature. The uncertainty in the NXB is  $\sim 3$  per cent (Tawa et al. 2008), and from an analysis of *ROSAT* data by Carrera, Fabian & Barcons (1997), we estimate that the cosmic variance due to point source clustering in the CXB is  $\sim 10$  per cent over this field of view. We also test the effect of metallicity from 0.2 to  $0.4 Z_{\odot}$  in the outer annuli and a range of  $\pm 10$  per cent in the column density. Each of these variations results in a change in temperature of  $\lesssim 10$  per cent for all annuli, and the individual systematic uncertainties are smaller than the Poisson uncertainties for all but the column density's effect on the central regions where the count rate is high. Finally, the normalization of the local thermal component, which could vary the most across the



**Table 4.** Estimated uncertainties in the radial temperature profile due to removing PSF corrections or changing normalizations of background components and spectral model parameters within the ranges given. Each parameter is varied independently and we present only the maximum of the upward and downward temperature shifts (in keV) for clarity. Best-fitting PSF-corrected temperatures and their statistical uncertainties are included for comparison.

Radius (arcmin)	$kT$ (keV)	Stat.	No PSF	NXB $\pm 3$ per cent	CXB $\pm 10$ per cent	Gal. $\pm 50$ per cent	$N_H$ $\pm 10$ per cent	$Z$ 0.2–0.4 $Z_\odot$
0–2.5	6.92	$+0.12$ $-0.12$	+0.08	<0.005	<0.005	<0.005	0.68	<0.005
2.5–6.0	7.85	$+0.45$ $-0.39$	–0.82	<0.005	<0.005	0.01	0.90	0.02
6.0–9.5	4.90	$+0.30$ $-0.27$	–0.01	0.02	0.04	0.03	0.41	0.05
9.5–13.5	3.22	$+0.47$ $-0.36$	–0.05	0.14	0.14	0.06	0.28	0.07
13.5–18.5	2.15	$+0.19$ $-0.18$	+0.09	0.06	0.17	0.06	0.15	0.11
>18.5	2.07	$+0.25$ $-0.23$	+0.02	0.10	0.21	0.06	0.13	0.12

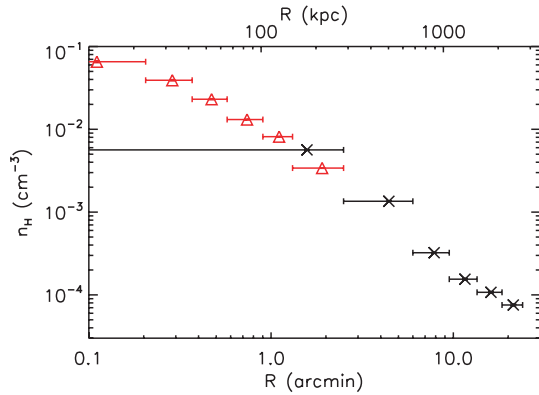


**Figure 8.** Comparison between *Chandra* (red triangles) and *Suzaku* (black crosses) density profiles. Error bars are smaller than the plot symbols.

cluster field of view because of the low Galactic latitude, actually has a very small effect on temperature fits above 1 keV.

Without spectral deprojection, the data from each annulus will be contaminated by emission from regions at larger radii. However, because the density profile falls so steeply and the thermal bremsstrahlung emission scales as the square of the density, the only noticeable effect is in the cluster core (e.g. fig. 3 of Sanders & Fabian 2007). This region is well within our innermost radial bin, so we do not expect significant errors due to the lack of deprojection of the *Suzaku* data.

As an additional check on the reliability of our temperature and density profiles, we compare the values from *Suzaku* with the *Chandra* observations used in the mass estimate. The high spatial resolution of *Chandra* allows for our central region to be divided into several annuli, with the average temperature in agreement with the *Suzaku* value. As shown in Fig. 8, the density profiles are also reasonably consistent between the two observatories, with a slightly steepening slope at the larger radii seen by *Suzaku*.

We can check the assumption of spherical symmetry used when deriving the mass profile, seeing if the emission is at least circularly symmetric by considering the projected profiles in each of the pointings separately. Fig. 9 shows the temperature, density and entropy profiles for each pointing. Here we do not include PSF corrections in order to keep each set of observations independent. The uncertainties are larger when splitting up the data, but the results from the separate pointings broadly overlap, and no single direction is consistently above or below the average temperature or density for

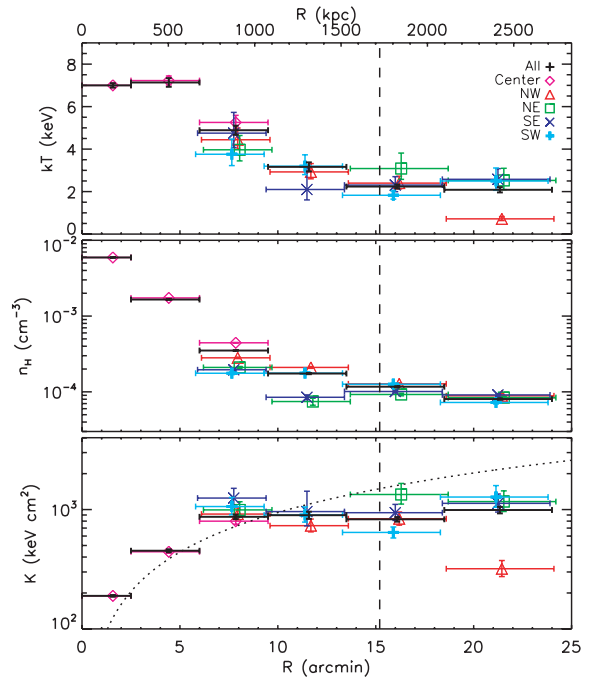


**Figure 9.** Comparison of temperature, density and entropy profiles in each direction. The temperature in the north-east (NE) direction is not well constrained from 9.5 to 13.5 arcmin due to a large amount of area excluded because of point sources, so the temperature and entropy points are not plotted in this region. Slight offsets are added to bin radii for clarity. The dotted curve in the bottom panel shows  $K \propto r^{-1.1}$ . The vertical dashed line shows our estimate of  $r_{200}$ , derived in Section 4.2.

every annulus. Scatter that is larger than the statistical uncertainties could be attributed to remaining point sources or minor asymmetry in the cluster.

The entropy seen in the outermost radial bin of the north-west (NW) pointing is significantly lower than nearby regions, mainly due to the temperature drop seen there. However, scatter between pointings or individual outliers are unable to explain the observed flattening of the entropy profile in the summed annuli. We plot a power law rising as  $r^{-1.1}$  to compare with the entropy profile predicted by analytical models of accretion shock heating and seen in some observations as well as numerical simulations (Tozzi & Norman 2001; Ponman, Sanderson & Finoguenov 2003; Voit, Kay & Bryan 2005). A small number of objects in the sample of Ponman et al.

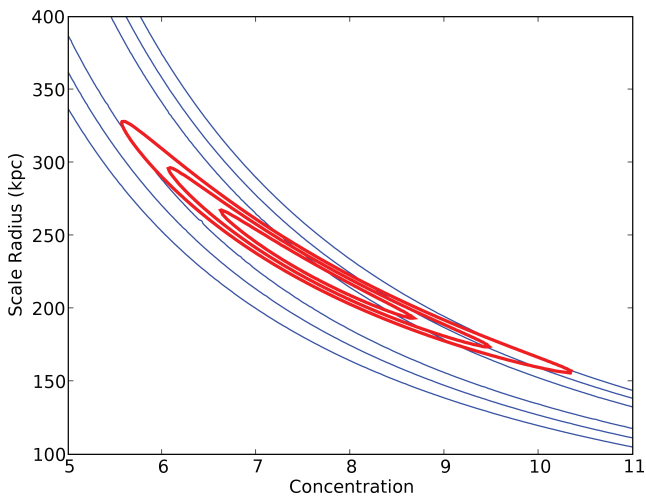


**Figure 10.** Likelihood contours for the concentration and scale radius parameters of the NFW fits, drawn at  $\Delta\chi^2 = 2.30, 6.17$  and  $11.80$ , corresponding to the  $1\sigma, 2\sigma$  and  $3\sigma$  confidence intervals, respectively. Thick red contours show the constraints from the combination of *Chandra* and *Suzaku* data, excluding the cluster core and the outermost annulus which is beyond the virial radius. Thin blue contours show the constraints without the *Suzaku* data for comparison.

(2003) have entropy curves that do not rise with radius. The observed and expected profiles agree at small radii, rising out of the core, but there is a clear entropy deficit in the outskirts of the cluster, perhaps indicative of infalling gas which is not dynamically stable. Our background model would have to be off by an order of magnitude, or the column density changed by a factor of 2, to increase the entropy in the outskirts to the predicted values.

For the estimates of the virial radius and mass, the method of fitting an NFW model to our temperature profile is an additional source of uncertainty. We have excluded the inner and outer regions where the assumption of hydrostatic equilibrium is likely to break down, but several variations of the temperature profile with these points included or excluded produce values for  $r_{200}$  consistent to  $\sim 10$  per cent. Similar values are also obtained when using only the *Suzaku* data, which has a large uncertainty in the central temperature due to PSF blurring. The wide radial span of this data set provides significantly tighter constraints on the NFW parameters than could be obtained with the *Chandra* data alone, as shown in Fig. 10. Data from the cluster core are still excluded in the contours plotted, though they might be used in a typical analysis. In either case with only *Chandra* data, the NFW scale radius is not well constrained since the data do not extend out that far, and the resulting estimate for  $r_{200}$ , and thus  $M_{200}$ , would be significantly larger than the values we obtain. We can also include the systematic uncertainties in the temperature profile within this process of fitting over NFW parameter space. Even with differences of  $0.5$ – $1$  keV between the FI and BI sensors which have similarly shaped but offset temperature profiles, changes in the best-fitting value of  $R_{200}$  are of order 10 per cent, giving a systematic uncertainty of 30 per cent for the determination of  $M_{200}$ .

We can also estimate the cluster mass independently of any model parametrization by plugging our density and temperature profiles directly into equation (1) and calculating gradients from the finite difference quotients of adjacent points. At large radii, the cumulative mass estimate using this method actually decreases, indicating that the hydrostatic assumption fails, and the uncertainties are large

because spatial gradients are taken between points separated by the wide thickness of annular bins. However, at the virial radius near 15 arcmin, the mass estimate agrees with that derived from the NFW model to within  $\sim 30$  per cent.

## 5 DISCUSSION

These are the first well-constrained measurements of the gas temperature profile beyond  $r_{200}$  for a rich and relaxed cluster, which we can now compare with model predictions and simulations. We see that there is a clear decline in temperature between  $0.3$  and  $1.5r_{200}$ , consistent with recent observational trends at growing radii (Vikhlinin et al. 2005; Pratt et al. 2007; Reiprich et al. 2008) and suggesting that conduction does not play a significant role on typical cluster time-scales. Roncarelli et al. (2006) measured the magnitude of the temperature drop in hydrodynamical simulations, finding a 40 per cent decline from  $0.3$  to  $1r_{200}$ , the same size found in the analytical treatment of Ostriker, Bode & Babul (2005). The drop observed in PKS 0745–191 over this radial range is closer to 70 per cent, but the general shapes of the profiles are similar.

The observed entropy profile deviates from expectations near the virial radius. Tozzi & Norman (2001) describe the effects on entropy of the accretion phases, including adiabatic infall, shock heating and adiabatic compression followed by cooling within the halo. Interestingly, we see evidence for an accretion shock beyond the virial radius in one direction (NW pointing in Fig. 9), suggestive of cool material falling inward along a filament. The change in entropy in the outer annulus of this region is not seen in the other directions, though the values there are still lower than would be expected from the typical increase of  $K \propto r^{1.1}$ .

The sharper decline in temperature than predicted and the flattening of the entropy profile in the outskirts suggest a need for non-thermal pressure support in order to maintain dynamic stability. The numerical simulations of Eke, Navarro & Frenk (1998) show a significant rise in the ratio of bulk kinetic energy to thermal energy beginning within the virial radius. Merger activity increases the turbulent pressure, and even though PKS 0745–191 appears relaxed morphologically, it should still be accreting matter in the outskirts. We note that the infall time-scale,  $t_f \sim (r^3/GM)^{1/2}$ , is of order 1 Gyr at the virial radius, and the time-scale set by the speed of sound,  $t_s \sim (r^2 m_H / \Gamma kT)^{1/2}$ , is several times larger.

Neumann (2005), studying the summed profiles of 14 nearby Abell clusters beyond  $r_{200}$ , argues that the ICM at large radii may not be in hydrostatic equilibrium, and that cool gas not seen in X-rays could increasingly dominate the baryon content in the outskirts. Afshordi et al. (2007) stacked *Wilkinson Microwave Anisotropy Probe* (WMAP) observations of a large sample of massive clusters and found a deficit in thermal energy in the outskirts from the Sunyaev–Zel’dovich (SZ) profile, also arguing for cool phase of the ICM. It is not well understood how these different phases would mix, and complicated gas physics would likely result. The assumption of hydrostatic equilibrium fails beyond the virial radius, as seen by the poorer temperature fits from mass modelling when the outermost temperature value is included. It is not obvious to what extent the ICM *within* the virial radius is not in equilibrium, but the entropy and temperature profiles suggest that non-thermal physics may be important in the outskirts of this cluster.

In Fig. 11, we plot the observed temperature profile against two models. The first is the expected temperature if the gas content traced the NFW distribution of dark matter, with a Keplerian velocity profile, i.e.  $T(r) \propto v(r)^2 \propto M(<r)/r$ . The second and more realistic case is for the projected X-ray temperature of gas arranged



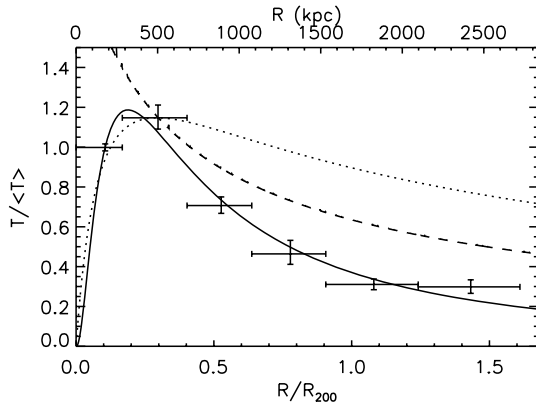


**Figure 11.** *Suzaku* temperature profile, normalized by the emission-weighted mean and compared with model profiles. The solid curve shows the parametrization of equation (3), also rescaled by the emission-weighted mean temperature that we observe. The dotted curve shows the temperature for gas tracing an NFW distribution, while the dashed curve shows a polytropic profile in hydrostatic equilibrium with an NFW potential. Both models are normalized to match the maximum observed temperature.

polytropically and in hydrostatic equilibrium with an NFW gravitational potential, as derived by Suto, Sasaki & Makino (1998). The outer temperatures we have observed are lower than those expected for reasonable values of the model parameters.<sup>2</sup> Additionally, we can fit the observed temperature profile using a simple parametrization

$$T(r) = T_1 \left( \frac{r}{r_s} \right)^\alpha \left( 1 + \frac{r}{r_s} \right)^\beta \text{ keV} \quad (3)$$

with best-fitting parameters  $T_1 = 135$ ,  $\alpha = 2.4$ ,  $\beta = -4.1$ , where  $r_s$  is the scale radius from the best-fitting NFW profile. We note that the normalization is related to the value of the temperature at this radius,  $T_1 = T(r_s)/2^\beta$ .

A possible explanation for the deficit of thermal energy seen at large radii is that infalling matter has retained some of its kinetic energy in bulk motion. If there is increasing pressure support from bulk motion, turbulence, or other non-thermal processes in the outer regions of the cluster, then the gravitational potential and thus total mass would be incorrectly estimated when assuming hydrostatic equilibrium. This effect would depend on the changes in both the temperature and its gradient, making estimation of the true mass difficult.

Alternatively, the peak temperature, seen in the second-innermost annulus, could be inflated due to non-thermal processes such as shock heating during infall. AGN heating is thought to play an important role in cool core clusters, and some excess energy could also heat the gas beyond the core. More observations are needed of this cluster and others to determine how well the self-similar scaling relations, which depend on the dominance of gravitational process in creating equilibrium, apply out to the virial radius.

The gas fraction we obtain is more consistent with previous results. At  $r_{200}$ ,  $f_{\text{gas}} = 0.13$ , lower than that found with *XMM* (Chen

et al. 2003), but similar to the *ROSAT* value of Allen et al. (1996). The trend of  $f_{\text{gas}}$  rising with radius is also seen in other clusters and in simulations (e.g. Eke et al. 1998; Vikhlinin et al. 2006), since the gas density distribution is less centrally concentrated than that for collisionless dark matter. The outermost measured value of  $f_{\text{gas}}$  is consistent with the mean cosmic baryon ratio derived from *WMAP* data and other cosmological observations,  $\Omega_b/\Omega_m = 0.165 \pm 0.006$  (Komatsu et al. 2009).

## 6 SUMMARY

We have presented the first measurements of the gas beyond the virial radius from a rich and apparently relaxed galaxy cluster. The temperature profile shows a significant decline at outer radii, while the entropy profile levels off. The spatially resolved temperature and density measurements out to and beyond the virial radius produce improved constraints on the mass and gas fraction profiles, though the observed temperature profile does show deviations from that expected from cluster gas in hydrostatic equilibrium with an NFW mass profile.

Observations of the outskirts of clusters offer a direct probe of their assembly history. The apparent shock front in one direction makes it clear that this cluster is still accreting material, likely along a filament. Evidence for non-thermal pressure support suggests that bulk motions from merger activity could be making a significant contribution to the gas energy in the outskirts of this cluster.

PKS 0745–191 is an ideal candidate for such observations, given its distance and luminosity. The angular size fits reasonably within a few pointings and the count rate is high enough for good spectral statistics. The low and well-constrained background levels of *Suzaku* are crucial for low surface brightness measurements like those presented here and by Reiprich et al. (2008). We expect that as the number of cluster observations in the *Suzaku* archive increases, these types of analyses will be able to probe the self-similarity of the outskirts of clusters. More studies at the virial radius, including X-ray observations, gravitational lensing, the SZ effect and numerical simulations, will provide a better understanding of the regime where hydrostatic equilibrium breaks down and clusters are still being assembled.

## ACKNOWLEDGMENTS

We thank James Graham, Thomas Reiprich, Steve Allen, Richard Mushotzky and Mark Bautz for helpful discussions and Roderick Johnstone for much assistance. MRG acknowledges a Herschel Smith Scholarship, HRR is supported by STFC and ACF thanks the Royal Society for support. This research has made use of data obtained from the *Suzaku* satellite, a collaborative mission between the space agencies of Japan (JAXA) and the USA (NASA).

## REFERENCES

- Afshordi N., Lin Y.-T., Nagai D., Sanderson A. J. R., 2007, *MNRAS*, 378, 293
- Allen S. W., Fabian A. C., Kneib J. P., 1996, *MNRAS*, 279, 615
- Allen S. W., Schmidt R. W., Fabian A. C., Ebeling H., 2003, *MNRAS*, 342, 287
- Allen S. W., Rapetti D. A., Schmidt R. W., Ebeling H., Morris R. G., Fabian A. C., 2008, *MNRAS*, 383, 879
- Anders E., Grevesse N., 1989, *Geochim. Cosmochim. Acta*, 53, 197
- Arnaud M., Pointecouteau E., Pratt G. W., 2005, *A&A*, 441, 893
- Carrera F. J., Fabian A. C., Barcons X., 1997, *MNRAS*, 285, 820
- Cash W., 1979, *ApJ*, 228, 939

<sup>2</sup> We set the parameter  $B_p$ , defined by Suto et al. (1998), equal to unity, and use the polytropic index derived from the best-fitting power laws to our data excluding the central region,  $\Gamma = 1.4$ . It is possible to obtain temperature profiles that decline as steeply as the observed one by increasing the value of  $B_p$ , though this would require truncating the gas distribution shortly beyond the regions we have measured. For the range  $\Gamma = 1.1$ – $2$ , the polytropic index used does not have a significant effect on the shape of the scaled profile.

- Chen Y., Ikebe Y., Böhringer H., 2003, *A&A*, 407, 41
- Comerford J. M., Natarajan P., 2007, *MNRAS*, 379, 190
- De Grandi S., Molendi S., 2002, *ApJ*, 567, 163
- Edge A. C., Stewart G. C., Fabian A. C., Arnaud K. A., 1990, *MNRAS*, 245, 559
- Eke V. R., Cole S., Frenk C. S., 1996, *MNRAS*, 282, 263
- Eke V. R., Navarro J. F., Frenk C. S., 1998, *ApJ*, 503, 569
- Evrard A. E., Metzler C. A., Navarro J. F., 1996, *ApJ*, 469, 494
- Fabian A. C. et al., 1985, *MNRAS*, 216, 923
- Frenk C. S. et al., 1999, *ApJ*, 525, 554
- Fujimoto R. et al., 2007, *PASJ*, 59, 133
- Irwin J. A., Bregman J. N., Evrard A. E., 1999, *ApJ*, 519, 518
- Ishisaki Y. et al., 2007, *PASJ*, 59, 113
- Kaiser N., 1986, *MNRAS*, 222, 323
- Kalberla P. M. W., Burton W. B., Hartmann D., Arnal E. M., Bajaja E., Morras R., Pöppel W. G. L., 2005, *A&A*, 440, 775
- Komatsu E. et al., 2009, *ApJ*, 180, 330
- Koyama K. et al., 2007, *PASJ*, 59, 23
- Liedahl D. A., Osterheld A. L., Goldstein W. H., 1995, *ApJ*, 438, L115
- Loken C., Norman M. L., Nelson E., Burns J., Bryan G. L., Motl P., 2002, *ApJ*, 579, 571
- McLaughlin D. E., 1999, *AJ*, 117, 2398
- Markevitch M., Forman W. R., Sarazin C. L., Vikhlinin A., 1998, *ApJ*, 503, 77
- Mewe R., Gronenschild E. H. B. M., van den Oord G. H. J., 1985, *A&AS*, 62, 197
- Mewe R., Lemen J. R., van den Oord G. H. J., 1986, *A&AS*, 65, 511
- Navarro J. F., Frenk C. S., White S. D. M., 1997, *ApJ*, 490, 493 (NFW)
- Neumann D. M., 2005, *A&A*, 439, 465
- O’Dea C. P. et al., 2008, *ApJ*, 681, 1035
- Ostriker J. P., Bode P., Babul A., 2005, *ApJ*, 634, 964
- Pointecouteau E., Arnaud M., Pratt G. W., 2005, *A&A*, 435, 1
- Ponman T. J., Sanderson A. J. R., Finoguenov A., 2003, *MNRAS*, 343, 331
- Pratt G. W., Böhringer H., Croston J. H., Arnaud M., Borgani S., Finoguenov A., Temple R. F., 2007, *A&A*, 461, 71
- Reiprich T. H., Böhringer H., 2002, *ApJ*, 567, 716
- Reiprich T. H. et al., 2008, preprint (arxiv:0806.2920)
- Roncarelli M., Ettori S., Dolag K., Moscardini L., Borgani S., Murante G., 2006, *MNRAS*, 373, 1339
- Sanders J. S., Fabian A. C., 2007, *MNRAS*, 381, 1381
- Sato K. et al., 2007, *PASJ*, 59, 299
- Schmidt R. W., Allen S. W., 2007, *MNRAS*, 379, 209
- Snowden S. L. et al., 1997, *ApJ*, 485, 125
- Snowden S. L., Mushotzky R. F., Kuntz K. D., Davis D. S., 2008, *A&A*, 478, 615
- Solovyeva L., Anokhin S., Sauvageot J. L., Teyssier R., Neumann D., 2007, *A&A*, 476, 63
- Suto Y., Sasaki S., Makino N., 1998, *ApJ*, 509, 544
- Tawa N. et al., 2008, *PASJ*, 60, 11
- Tozzi P., Norman C., 2001, *ApJ*, 546, 63
- Vikhlinin A., Markevitch M., Murray S. S., Jones C., Forman W., Van Speybroeck L., 2005, *ApJ*, 628, 655
- Vikhlinin A., Kravtsov A., Forman W., Jones C., Markevitch M., Murray S. S., Van Speybroeck L., 2006, *ApJ*, 640, 691
- Voigt L. M., Fabian A. C., 2006, *MNRAS*, 368, 518
- Voit G. M., 2005, *Rev. Mod. Phys.*, 77, 207
- Voit G. M., Kay S. T., Bryan G. L., 2005, *MNRAS*, 364, 909
- White S. D. M., Navarro J. F., Evrard A. E., Frenk C. S., 1993, *Nat*, 366, 429
- Zhang Y.-Y., Finoguenov A., Böhringer H., Ikebe Y., Matsushita K., Schuecker P., 2004, *A&A*, 413, 49

This paper has been typeset from a  $\text{\LaTeX}$  file prepared by the author.